Role of porosity in the induced failure mechanisms of isotropic ice under three-points flexural loading

David Georges, Dominique Saletti, Maurine Montagnat, Pascal Forquin, Hubert Maigre

Role of porosity in the induced failure mechanisms of isotropic ice under three-points flexural loading

David Georges[1], Dominique Saletti[1], Maurine Montagnat[2,3], Pascal Forquin[1], and Hubert Maigre[4]

[1] Univ. Grenoble Alpes, CNRS, Grenoble INP, 3SR, F-38000 Grenoble, France
[2] Univ. Grenoble Alpes, CNRS, Grenoble INP, IGE, F-38000 Grenoble, France
[3] Univ. Grenoble Alpes, Université de Toulouse, Météo-France, CNRS, CNRM, Centre d'Etudes de la Neige, Grenoble, France
[4] INSA-LYON, CNRS, LaMCoS, UMR5259, F69621 Villeurbanne, France

The knowledge of the flexural strength of ice is essential to prescribe the interaction with building structures in various environments such as off-shore platforms or icy roads in the Great North.
Microstructural properties of polycrystalline ice, mostly grain size and porosity, can strongly vary in natural ice and impact the mechanical response. There exist currently no bending experimental results that incorporate a robust characterization of these microstructural properties.
In most fragile materials, such as concrete and rocks, pores often act as critical defects to trigger failure. Therefore, the porosity (pore size and shape distributions, density) can be considered as a major characteristic of the microstructure.
In the present work we aim at (i) providing a robust set of bending experiments on well-controlled polycrystalline ice microstructures and (ii) provide a robust and accurate method for accessing the bending properties of ice through defect characterization. To do so, bending experiments were done on isotropic polycrystalline ice with the same grain size and shape distribution and two different porosity properties. Porosity was characterized at a relatively high resolution (down to 7μm) by micro-computed X-ray tomography (μCT).
As classically done, the bending failure stress measurements have been statistically analyzed by means of the Weibull model. It results that, in situations were porosity follows a multi-modal distribution or a distribution too far from a Weibull one, this statistical approach is not well appropriate. An alternative is suggested that makes use of the accurate microstructure characterization from μCT. Providing that the Griffith/Irwin failure criterion can be applied, the measured pore distribution gives access to the prediction of a critical stress for defect activation. When compared with experimentally measured failure stress, this prediction enables to discriminate the defect population responsible for failure and highlight a volume effect on the behavior.
As a result, we show that care should be taken when attempting to use the Weibull model to calibrate mechanical tests with complex and heterogeneous loadings (such as dynamic loadings) and complex microstructures. To make direct use of high resolution characterizations of the defect microstructure, when available, offers a more robust, accessible, and accurate predictability of the flexural strength.

Keywords failure strength; polycrystalline ice ; porosity; micro-CT characterization

1 Introduction

The flexural strength of polycrystalline ice is a material property of interest for many engineering applications. Floating ice covers are for instance commonly used as ice bridges and roads in the cold regions, in this case the bearing capacity of ice is directly involved. In these regions, the impact of icebergs and/or ice floes with icebreaker ships and offshore structures are also frequent and can pose a serious threat.

Consequently, studies focusing on ice flexural behavior have been conducted, especially during the period 1960-1995. Although Schwarz et al. 1981 attempted to establish experimental recommendations to determine ice properties, most of these studies did not use similar experimental procedures (cantilever beam test, three or four-points bending tests) applying different external forcing (in particular loading rate and temperature) and using different types of ice samples (lab made / natural, microstructure, geometry, etc.). Timco et al. 1994 gathered several

thousands of measurements from 19 different studies on sea ice and fresh-water columnar ice. All these results put together suffer from a significant scattering.

On top of that, a systematic lack of information about the microstructural properties prevent from connecting the flexural strength (usually took as the measured stress to failure) scattering and the defect distribution in the microstructure. Indeed, brittle-like materials subjected to a quasi-static tensile stress field are expected to fail at random stresses due to the development of a single crack triggered from a microstructural defect (Jayatilaka et al. 1977). As shown by (Hawkes et al. 1972; Schulson, Lim, et al. 1984; Druez et al. 1987) and reviewed in (Schulson and Duval 2009), ice below -10°C can be mechanically considered as a brittle material when loaded at rates above 10^{-7} s^{-1}. The defect can be a micro-crack, an inclusion, a pore, a sintering defect or an impurity for instance, and its critical stress of activation (equivalent to the failure stress in quasi-static conditions) is supposed to be related to its nature and/or its size.

So far, probability distribution functions have been used to describe the strength of brittle materials. Amongst them, the Weibull distribution (Weibull 1939) is state of the art for mechanical design procedure although strength data associated with the materials of concern are not necessarily distributed according to a Weibull statistic law. To our knowledge, only Tozawa et al. 1986, B. L. Parsons et al. 1991 and B. Parsons et al. 1992 described the failure stresses of ice samples with a statistical approach by applying a Weibull or a double exponential distribution for different sets of bending experiment results. Again, in these works, little information is provided concerning the microstructural properties of the tested ices. Amongst the obtained results, B. Parsons et al. 1992 showed that the effect of volume could not be described by the Weibull model, what is also of concern for other brittle materials. Indeed, as shown by Danzer et al. 2007 or even Forquin, Rota, et al. 2004 for ceramics, the Weibull distribution reliability is restricted to volumes in relation with the active defect size distribution. A more robust method to provide accurate predictions of the active defect characteristics in brittle materials, and especially ice in the present work, is thus required.

In line with the approach presented by Forquin, Blasone, et al. 2021, 3D characterizations of the defect distribution within a material is considered here as an alternative approach to evaluate the active defect population relatively to the forcing. In the present study, ice is the brittle material under consideration, whose defect population is made of pores of various size and density (in the sense of number per unit volume). A full 3D characterization is obtained by micro Computed Xray Tomography (μCT) analyses performed over large laboratory grown ice samples, with different porosity, whose size and shape are characterized down to a resolution of 7 μm. The effect of porosity on the flexural strength is explored thanks to a set of well-constrained experimental tests. Then, a comparison is given between a Weibull statistical approach that predicts the critical defect population from the experimental measurements, and a direct approach that uses the full 3D characterization of the pore distributions such as in (Forquin, Blasone, et al. 2021).

2 Material

2.1 Sample growth

Samples are made of polycrystalline granular ice grown in the laboratory with a microstructure with either a low porosity (LP)($\approx 1-2\%$) or a high porosity (HP)($\approx 7-10\%$). Both types of microstructure are obtained by a growth technique inspired from (Barnes et al. 1971) and described in (Georges et al. 2021). Samples are grown from isotropic seeds made of crushed ice (with a maximum particle diameter of 2 mm) immersed in water at 0°C. The slurry is placed on a Peltier element (-15°C), in a 0°C room, to grow gently from bottom to top. To obtain the LP microstructure, the crushed ice is pumped before adding the water. In order to produce the HP microstructure, the air trapped between the crushed ice grains is kept (no pumping). Samples LP show no visible porosity and are slightly opaque, whereas large pores are visible in samples HP. After demoulding, samples are stored during 24 hours in a 0°C environment. This annealing stage enables the relaxation of the freezing stresses and to homogenize the grain size by normal grain growth. The length of the cylindrical samples, prior to machining, is about 20-25 cm. The few

samples that showed pores of size exceeding 10 mm were removed.

2.2 2D characterisation

In order to provide a detailed 2D characterisation of the microstructures, some LP and HP samples, not tested but assumed to be representative of the whole sets, were machined in thin square sections of approximately 50×50 mm^2 and 0.3 mm in thickness. An Automatic Ice Texture Analyzer (AITA) (Wilson et al. 2003) was used to measure the optical axis (the [0001] **c**-axis of the hexagonal crystal cell of ice) orientations all over the obtained thin sections. Data so obtained enables to access the 2D crystalline structure of the samples, i.e. the crystals size and shape and their crystallographic orientations. The **c**-axis orientations are measured at a resolution of 20 μm, with about 3° of angular resolution (Wilson et al. 2003).

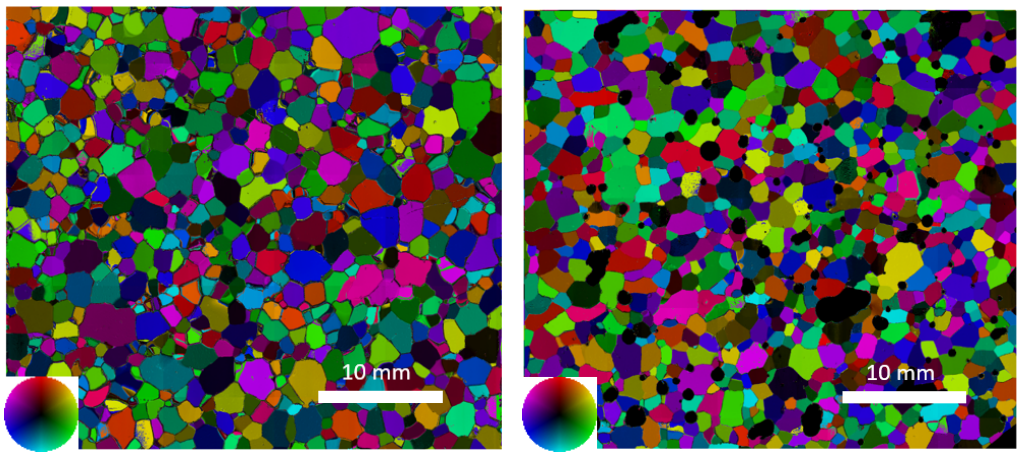

Figure 1: Microstructures colour-coded with the **c**-axis orientation for low porosity (LP) (a) and high porosity (HP) (b) samples. Data are obtained with the Automatic Ice Texture Analyzer from thin sections. Rounded black areas correspond to pores in (b).

Sections analyzed with the AITA, figure 1, show isotropic textures, i.e. a rather equiaxed grain shape and an isotropic distribution of **c**-axis orientations. Grain areas were measured by extracting grain contours with morphological tools from the orientation color-coded images. The grain size distribution is Gaussian and the mean grain diameter ranges between 1 and 2 mm for both types of samples.

2.3 3D characterisation

X-ray Micro Computed Tomography, μCT, is a convenient non destructive method to evaluate the 3D microstructure of heterogeneous materials and more specifically to quantify the size, shape and space distributions of pores. In order to characterize these distributions and their statistical significance, scans with different resolutions and geometries were made on several HP and LP samples.

2.3.1 Description of the μCT configuration (TomoCold)

Scans were performed with the TomoCold DeskTom130 (RX Solutions) tomograph located in a cold room set at -20°C at the CNRM-CEN (Centre National de Recherche Météorologique - Centres d'Etudes de la Neige), Grenoble. The source is composed of a 150 kV RX tube with a focal size that can reach 5 μm and of a flat panel detector with an active surface of about 1920×1536 pixels (physical pixel size of 127 μm). In order to provide a meaningful statistical distribution of pores, including the largest ones, large cylindrical samples of $\varnothing \times h = 45 \times 120$ mm^3 were analysed (later called samples LP$_T$(L) or HP$_T$(L)) with a voxel size of 27 μm. Full scans for LP$_T$(L) and HP$_T$(L) samples are reconstructed from four stacks scanned at different sample heights (by a vertical translation of the source and detector). Smaller volumes of $\varnothing \times h = 12.7 \times 9.2$ mm^3 (samples LP$_T$(S) or HP$_T$(S)) were analyzed to a higher resolution of 7 μm voxel size. For the latter, partial scans were done out of samples of $\varnothing \times h = 20 \times 40$ mm^3. This higher resolution was necessary to better identify the smallest pore population. Specific settings of the μCT analyses

are listed in table 1.

	Voxel size (μm)	Current/Voltage (μA/kV)	Radiographies per projection	Duration of analysis
$LP_T(S)01$	7	117/60	4	1h36
$LP_T(S)02$	7	117/60	4	1h36
$LP_T(S)03$	7	117/60	8	3h12
$LP_T(L)01$	27	238/60	2	1h04
$LP_T(L)02$	27	238/60	2	1h04
$LP_T(L)03$	27	238/60	2	1h04
$HP_T(S)01$	7	117/60	4	1h36
$HP_T(S)02$	7	117/60	8	3h12
$HP_T(L)01$	27	238/60	2	1h04
$HP_T(L)02$	27	238/60	2	1h04
$HP_T(L)03$	27	238/60	2	1h04

Table 1: Settings of the μCT analyses performed with the TomoCold. *LP* and *HP* stands for Low and High Porosity respectively. (S) and (L) for Small and Large area of analysis. See text for more details.

2.3.2 Image post-processing

For every scan a 3D image was reconstructed from the acquired radiographs. A ring filter with a 20 voxel kernel was applied in order to remove ring features that are acquisition artefacts. After reconstruction, scans were composed of approximately $4500 \times 1660 \times 1660$ voxels for large samples and $1300 \times 1800 \times 1800$ voxels for small ones, whose value spreads out between 0 (black) and 65536 (white). A contrast enhancement was done prior to conversion into 8 bit images to obtain reproducible grey level histograms. This operation allowed to apply the same threshold method for each scan of the same sample type (HP or LP). Typical images (8 bits) scanned with a voxel size of 7 μm and 27 μm are shown on figure 2. Figures 3 represents the grey level distribution obtained for the two sample types. Both show similar distributions whatever the scanning resolution.

The segmentation phase, that enables to separate ice and air into binary images requires to separate the two grey-level distributions that result from the raw scans. This threshold step is crucial, in order to minimize the segmentation errors that could lead to an over or under estimation of the porosity by artificially enlarge or reduce the volume occupied by air (or ice, although it is here the dominant phase), especially for small features that are particularly sensitives to the threshold value.

We assume that both distributions can be approximated by Gaussians, and the threshold value is chosen at the intersection between the two Gaussian fitting of each phase (in red and yellow for air and ice respectively, figure 3). Finding an accurate threshold is more subtle for histograms associated to LP samples, as the pore density and size are much smaller. A pseudo-maximum for the air phase is therefore manually determined.

The obtained binary images are treated via SPAM (The Software for the Practical Analysis of Materials) (Andò et al. 2017), a Python package currently in development in the laboratory 3SR (Sols Solides Structures), Grenoble. During this step, each group of isolated or aggregated black voxels (air) is labelled. Some small labels can be artefacts from Gaussian noise (due to photon scattering during μCT acquisition) and it is preferable to set a minimal label size. Consequently, only labels corresponding to more than 10 voxels, $\sim 2 \times 10^{-4}$ mm^3 ($\sim 3.4 \times 10^{-6}$ mm^3) for a voxel size of 27 μm (7 μm) here, were taken into account and considered as pores.

Pores are characterized by their equivalent radius r_{eq} defined as the radius of a sphere whose volume equals the pore volume. A coefficient of sphericity Ψ is used to characterize the geometry of the pores. r_{eq} and Ψ are given by :

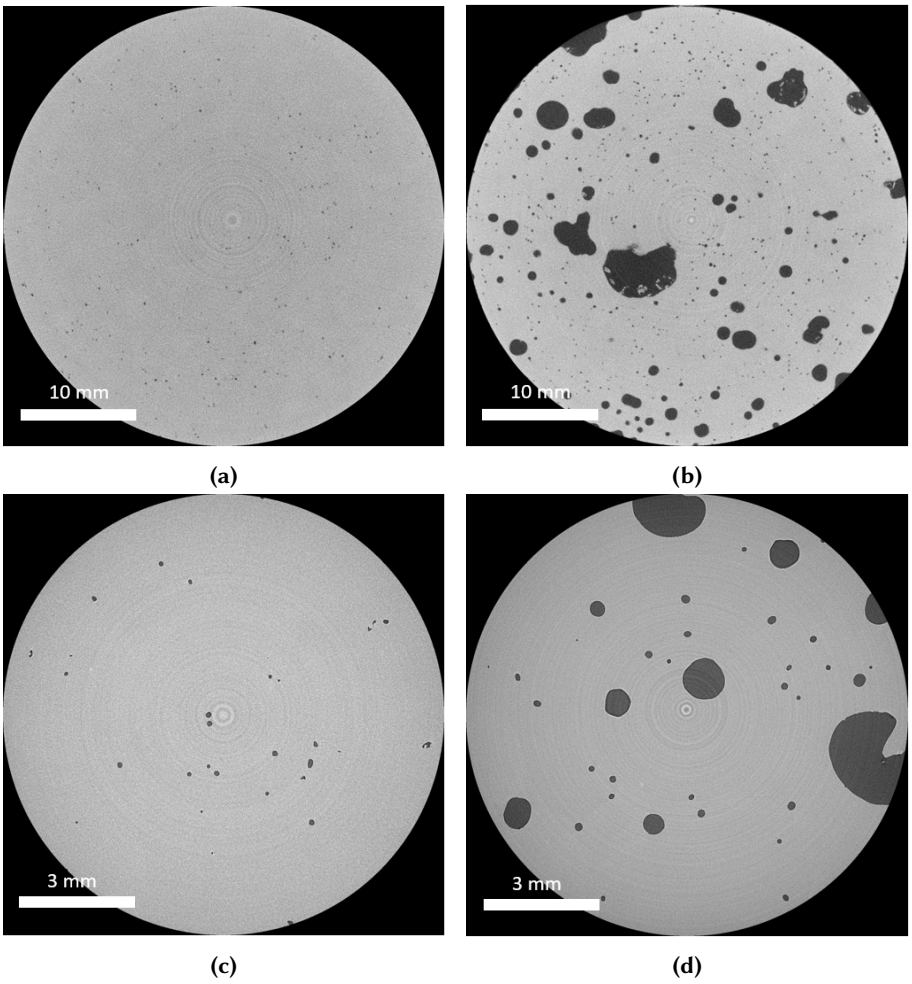

Figure 2: 2D slices (8 bits) perpendicular to the sample axis from scans (a) $LP_T(L)01$, (b) $HP_T(L)01$, (c) $LP_T(S)01$ et (d) $HP_T(S)02$.

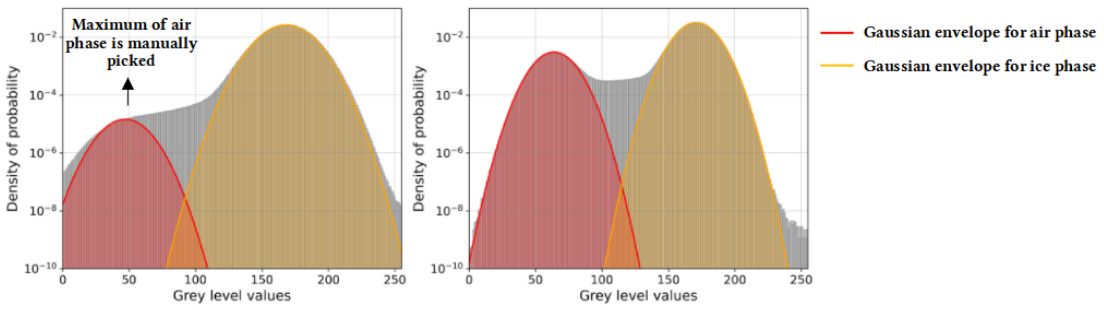

Figure 3: Probability density function of voxel grey levels for (*Left*) LP and (*Right*) HP samples.

$$r_{eq} = \sqrt[3]{\frac{3V_p}{4\pi}} \quad \text{and} \quad \Psi = \frac{\pi^{1/3}(6V_p)^{2/3}}{A_p} \tag{1}$$

with V_p and A_p the volume and the area of the ideal ellipsoid fitting the porosity. The technique described by Ikeda et al. 2000 was applied to estimate the length of the principal axes of this ellipsoid. A coefficient of sphericity close to 1 indicates almost spherical pores while pores are close to flat when the coefficient tends to 0. We can also collect the coordinates (x, y, z) of the center of mass of each pore in the scanned volume.

2.3.3 Pore size and shape distributions

The number of scans evaluated, for both types of microstructure, allowed to verify that the growth procedure led to reproducible microstructures. Figure 4 represents the mean cumulative

distribution of pore size (r_{eq}) for LP (in blue) and HP (in red) microstructures. These distributions gather results obtained from scans at 7 and 27 μm. The pore shape distribution is shown in figure 5. Scans at 7 μm enabled to identify pores of equivalent radius as low as 0.009 mm. From these distributions, we classified the pores into three different populations. The population **L** (Large) is characterized by large spherical pores ($r_{eq} > 0.3$ mm, and Ψ close to 1) and is mainly observed in HP samples (only 12 pores of this population have been identified in LP samples). Pores whose equivalent radius is between 0.1 and 0.3 mm belong to population **M** (Medium). The pores belonging to this population present in average a lower sphericity coefficient ($0.4 \leq \Psi \leq 1$) than population **L**, for both microstructure types. Population **S** (Small) includes pores whose equivalent radius is lower than 0.1 mm.

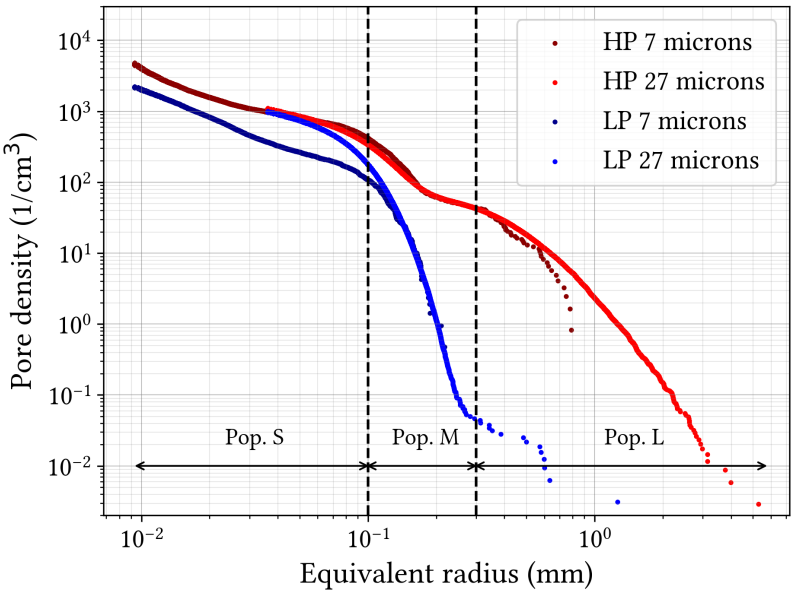

Figure 4: Mean cumulative distribution of pore size (r_{eq}) for LP (blue) and HP (red) microstructures. The results from scans at 7 microns (dark distributions) and 27 microns are superimposed.

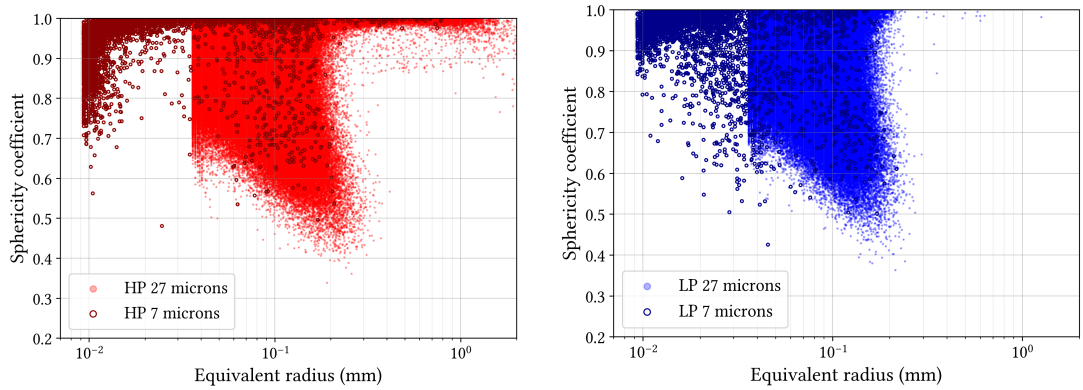

(a) **(b)**

Figure 5: Sphericity coefficient of pores from (a) LP and (b) HP samples. Colored (blue and red) points correspond to the results from one sample of each scanned at 27 microns. Darker and empty circles represent the sphericity coefficient of all pores detected in all samples scanned at 7 microns.

3 Bending tests

3.1 Sample design

From the grown cylindrical samples (see section 2.1), parallelepipedic samples were milled in a cold room at -10°C. Milling allowed to ensure that the loaded faces have a parallelism default at

least lower than 0.01%.

Pores are considered here as the active defects in these ice microstructures. Samples therefore had to be sized in order to contain a statistically representative number of pores of the population of interest. HP samples for instance were oversized in order to make sure that there are enough pores from population **L** in the tested volume. LP samples, that contain smaller pores were given a smaller size. Sample dimensions were $L \times h \times b = 140 \times 40 \times 20$ mm^3 for the HP microstructure (26 samples) and $L \times h \times b = 60 \times 20 \times 10$ mm^3 for the LP microstructure (29 samples). 6 small HP samples (called HPS) ($L \times h \times b = 60 \times 20 \times 10$ mm^3) were also manufactured in order to test a volume effect on the failure strength.

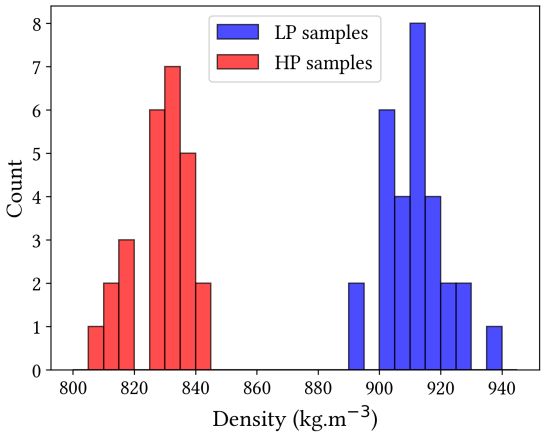

Figure 6: Density of LP and HP bending samples in their final dimensions.

3.2 Experimental device and procedure

Experiments on HP samples were conducted in the 3SR laboratory (Grenoble, France) during a first campaign. A second experimental campaign, where the LP and HPS samples were tested, was led by using the LaMCoS (Lyon, France) facilities. The experimental procedure was kept as similar as possible between both campaigns. In both cases, a three-points bending device was mounted in an uni-axial press controlled by displacement rate. The presses were coupled with a climatic enclosure supplied with liquid nitrogen in order to regulate the sample temperature during the tests. The choice of the test temperature (-30°C) was made to limit potential plastic deformations during the experiments (Schulson and Duval 2009).

Prior to loading, samples were stored in a freezer (-30°C) located nearby the climatic enclosure in order to reduce to a few second the time of exposition to ambient temperature (20°C) during the sample transfer. Markers (3SR) or stops made of tape (LaMCoS) were used to facilitate the setting of ice samples and also to ensure an optimal position with respect to the loading device. After several openings/closings of the climatic enclosure, frost starts to develop on the loading supports that could lead to a parallelism mismatch between the loading device and the sample. The supports were therefore systematically brushed prior to testing. After failure, fragments of tested samples were carefully kept for observations in the cold room.

During the second experimental campaign (LaMCoS) we used a high-speed camera (camera Phantom V710, 80000 fps) put in front of the climatic enclosure (see figure 7) to study the failure kinetic, i.e. (i) to verify that the fracture plane was located in the volume subjected to tensile loading and (ii) when possible, to detect the pores responsible for the fracture.

3.2.1 Loading rate

The ductile to brittle transition of polycrystalline ice under tensile loading depends on the strain-rate and occurs at about 10^{-7} s^{-1} at -10°C (Schulson 2001). The results of the bending tests are analysed in the frame of the linear elastic theory of beams, what assumes an elasto-brittle behavior of the ice samples. In order to secure a purely brittle failure, the displacement rate was set at $\delta = 4 \times 10^{-6}$ m.s^{-1} for the campaign at 3SR. Regarding the dimensions of HP samples and according to the linear elastic theory for three points bending, the resulting strain-rate can be

Figure 7: Left: High speed camera pointing toward the climatic enclosure (LaMCoS). Right: Three-points bending devices.

estimated by:

$$\dot{\varepsilon} = \frac{6h\delta}{L'^2} = 2.7 \times 10^{-5} s^{-1} \tag{2}$$

with $L' = 120$ mm, the distance between the bottom supports and h the specimen height. The applied strain-rate is almost two magnitudes faster than the expected ductile to brittle transition at -10°C, although it will be shown in section 3.3 that the loading path of several samples does not show a perfectly linear behavior. Therefore, during the second campaign at LaMCoS, the displacement rate was increased to $\delta = 5 \times 10^{-5}$ m.s^{-1}, i.e. $\dot{\varepsilon} = 2.4 \times 10^{-3}$ s^{-1} according to equation 2. From (Timco et al. 1994; Petrovic 2003; Timco and Weeks 2010), ice flexural strength does not depend on the strain-rate as long as the loading is purely elastic. The difference in strain-rate between both campaigns is thus expected to have a negligible effect except if plasticity indeed comes into play.

The flexural strength σ_f is obtained from the maximum force F_{max} measured just before failure by:

$$\sigma_f = \frac{3F_{max}L'}{2bh^2} \tag{3}$$

with b the specimen width.

3.3 Results

3.3.1 Validity of tests

The loading curves measured during the two experimental campaigns are presented in figure 8. The times to failure measured during the 3SR campaign present a large variability, from 20 s to 110 s. Load drops are sharp and sudden, as expected during a purely brittle failure. Nevertheless, for tests with time to failure exceeding 70 s, the loading path is not linear. This phenomenon is probably related to contact issues. Another origin, less likely regarding the applied stress rate, could be the occurrence of some plastic deformation during the loading. Besides the fact that no evidence of plasticity could be found in the ice samples, plastic deformation does not disturb the post-processing as long as plasticity is bounded to areas near contact points. Local maxima (slight load drops) are also visible on the loading curve of HP20 sample. The most likely explanation is the breaking or motion of frost particles on the bottom or/and upper supports.

During the LaMCoS campaign, performed at a higher loading rate, time to failure occurred in a narrower range, between 15 and 20 s (except for samples LP02 and LP07). For every test, the load drop is sharp and sudden, as expected during a purely brittle failure. As an illustration of a classical test behaviour, images taken from the high-speed camera at different critical times of the failure for LP04 sample are shown on figure 9. The fracture planes seem to result from the propagation of a single crack triggered in the bottom part of the sample submitted to a tensile stress. Narrow micro-cracks can also be observed just below the upper contact area. These micro-cracks seem to be local enough not to disturb the tensile stress field in the bottom part,

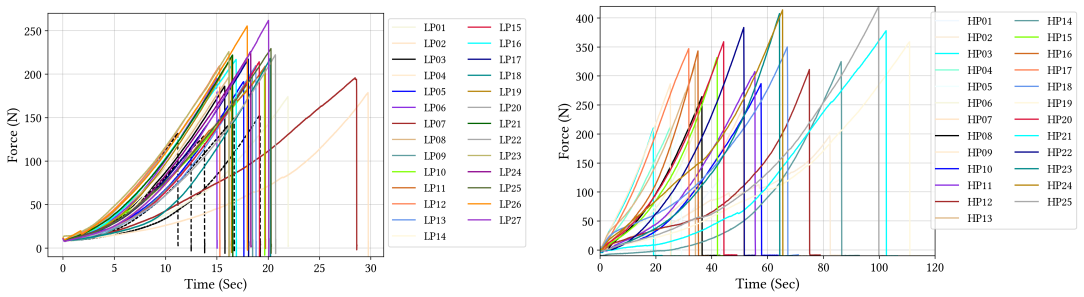

(a) **(b)**

Figure 8: Loading curves from the campaign in (a) LaMCoS and in (b) 3SR. Black dashed curves in figure (a) show the HPS samples tested during the campaign in LaMCoS.

where the main crack is activated. None of these micro-cracks were seen later on the post-mortem samples, and therefore most likely healed between the test and the analysis in the cold room. We expect similar micro-cracking to have occurred in the HP samples during the first campaign. The fracture surfaces of post-mortem samples present a low roughness and cracks seem to have

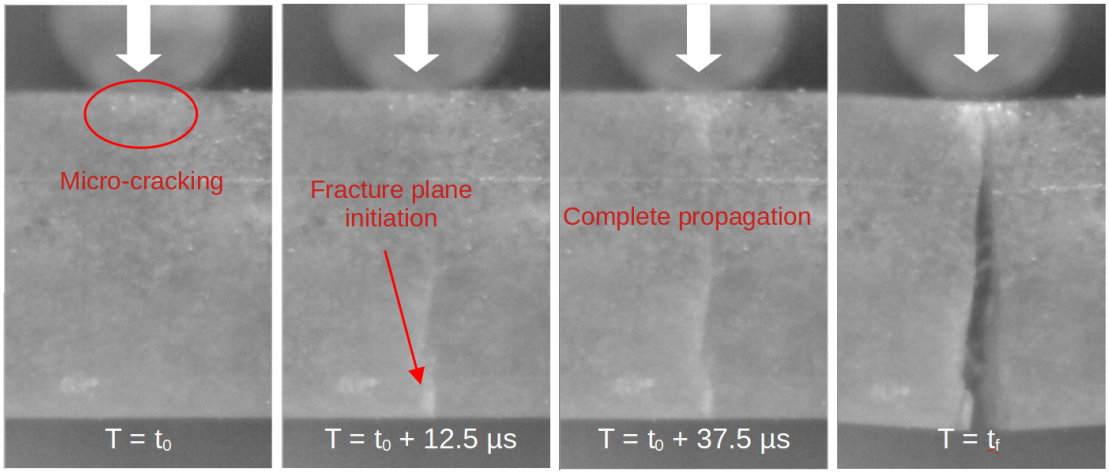

Figure 9: Key moments of the LP04 sample failure (images from the high-speed camera Phantom). The loading axe is symbolised by the white arrow on the upper support.

propagated without noticeable shift of direction, indicating that other microstructure defects (most likely pores in our case) did not interfere on the crack propagation. We observed two main configurations: (i) a crack initiates along the loading direction (i.e. where the maximal tensile stress is reached), figure 10(a), and propagates straight and vertically, (ii) a crack is triggered at the side of the loading direction (figure 10(b)) and the propagation occurs at an angle θ with respect to the loading direction and eventually reaches the upper support. This second type of fracturing mode was more commonly encountered in HP samples.

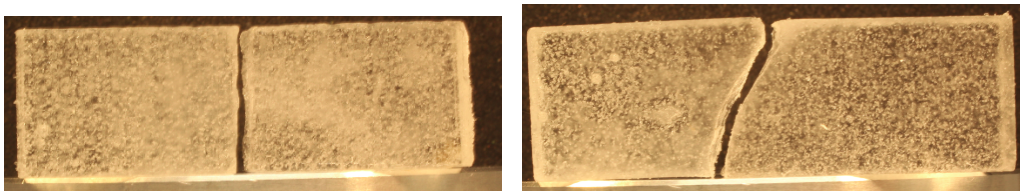

(a) **(b)**

Figure 10: Photos of (a) LP08 and (b) LP02 post-mortem samples.

3.3.2 Failure stresses

The forces measured at failure are listed in table 2 for both experimental campaigns. The flexural strength is calculated using equation 3. The mean flexural strengths are $\sigma_w(HP) = 1.76 \pm 0.42$

MPa for HP samples (HPS samples excluded) and $\sigma_w(LP) = 3.96 \pm 0.37$ MPa for LP samples. An average value of $\sigma_w(HP) = 2.54$ MPa is also measured from the few HPS samples tested in conditions similar to the LP samples. LP samples show a significantly higher flexural strength than HP samples, whatever the experimental conditions considered. HP samples tested in the 3SR conditions show a lower strength than smaller HPS samples tested in the LaMCoS conditions, what is coherent with an expected sample size effect.

LaMCoS campaign				3SR campaign			
Spec Id	T_f (sec)	F_{max} (N)	σ_F (MPa)	**Spec Id**	T_f (sec)	F_{max} (N)	σ_F (MPa)
LP01	22	174	3.26	HP01	43	123	0.69
LP02	30	179	3.35	HP02	82	197	1.11
LP03	16	186	3.49	HP03	19	210	1.18
LP04	18	189	3.55	HP04	25	214	1.20
LP05	18	191	3.59	HP05	29	216	1.21
LP06	15	195	3.66	HP06	36	231	1.30
LP07	28	196	3.67	HP07	51	246	1.38
LP08	16	196	3.68	HP08	37	264	1.49
LP09	18	204	3.82	HP09	58	287	1.61
LP10	20	206	3.87	HP10	25	286	1.61
LP11	20	209	3.92	HP11	56	308	1.73
LP12	15	210	3.93	HP12	75	311	1.75
LP13	19	210	3.93	HP13	34	320	1.80
LP14	16	211	3.96	HP14	86	325	1.82
LP15	19	214	4.01	HP15	42	332	1.87
LP16	17	217	4.07	HP16	35	343	1.93
LP17	18	217	4.07	HP17	32	347	1.95
LP18	20	218	4.09	HP18	67	350	1.97
LP19	16	219	4.11	HP19	44	359	2.02
LP20	16	220	4.13	HP20	111	359	2.02
LP21	17	222	4.16	HP21	103	378	2.13
LP22	21	222	4.17	HP22	52	383	2.16
LP23	16	226	4.23	HP23	64	407	2.29
LP24	18	226	4.24	HP24	65	414	2.33
LP25	20	229	4.30	HP25	100	418	2.35
LP26	18	255	4.79				
LP27	20	261	4.91				
HPS01	12	114	2.14				
HPS02	14	130	2.43				
HPS03	11	133	2.48				
HPS04	17	149	2.80				
HPS05	19	153	2.88				

Table 2: Bending tests results, with T_f: Time to failure, F_{max}: Maximal force to failure, σ_F: Flexural strength (maximal stress to failure).

3.3.3 Influence of porosity on the failure process

The images obtained from the high-speed camera and the observation of the fracture surfaces enable to discriminate the pore involved in the cracking process, in the case of HP samples, where the pores are the largest. They can help understanding the role of pores in the initiation of

the fracture planes.

Photos of the fracture surfaces of samples HP01, HP10 and HP23 are shown in figure 11. For sample HP01, three large pores whose diameter exceeds 10 mm are visible (black circles) and the failure stress of this sample is noticeably low (0.69 MPa). No other samples presented as large pores on their fracture surfaces, and sample HP01 should have been eliminated prior to testing on the basis of the sample selection criteria (see section 2.1). On the failure surface of sample HP10 (failure stress of 1.61 MPa), a pore of about 5 to 7 mm diameter (black circle) is observed in the area presumably submitted to a tensile stress. The other visible pores do not exceed 1 mm in diameter. Sample HP23 shows one of the highest measured failure stress (2.29 MPa). In its failure surface there is no pores larger that 1 mm in diameter. These three examples are representative of observations made for the whole set of HP samples; a low failure stress is associated with the presence of large pores on the fracture surface. However this image analysis remains qualitative.

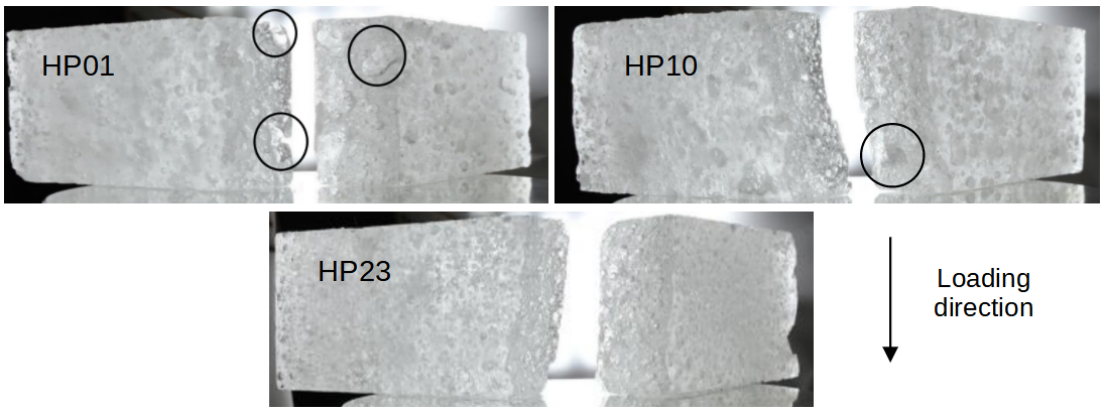

Figure 11: Photos of (a) HP01, (b) HP09 and (c) HP23 post-mortem samples.

Images from the high-speed camera complement this observation by enabling us to observe the crack triggering and the propagation path. An example is given for sample HPS03 in figure 12(a). The first image ($T = t_0$) shows the sample several microseconds before the fracture initiation, with a pore visible on the left side of the loading axis. On the next image ($T = t_0 + 12.5$ μs), a crack seems to develop from this pore to then propagate up to the zone in direct contact with the upper support ($T = t_0 + 25$ μs). Although only illustrated here for sample HPS03, pores were systematically observed on the crack path of HPS samples, in the tensile stress field area (cf figure 12(b)). These images, 2D and of high opacity, may not be a quantitative proof but they strengthen the hypothesis that pores are the active defects during fracturing.

4 Characterization of the defect population with the Weibull model

The Weibull model enables the association of a failure probability distribution with a critical stress of solicitation, assuming that activated defects in the material follow a Weibull distribution. In the following, we will check the applicability of the Weibull model and its ability to identify the pore population responsible for the sample failure.

4.1 The Weibull distribution

Quasi-brittle or brittle materials subjected to a quasi-static tensile loading fail at random stresses. For a given applied stress the failure occurs with a probability P_f. This probability is related to the stress field inside the sample and to the properties of the defect distribution (nature, size, density, orientation, etc.) in the sample volume V. In the following, and based on the experimental results, the hypothesis is made that the pores are the active defects in the ice samples studied.

The failure statistic model suggested by Weibull 1939 lies on the hypothesis of the weakest link. In other words, the failure of the weakest element in a volume, once its critical stress of activation reached, induces the ruin of the whole structure. This hypothesis is valid provided that

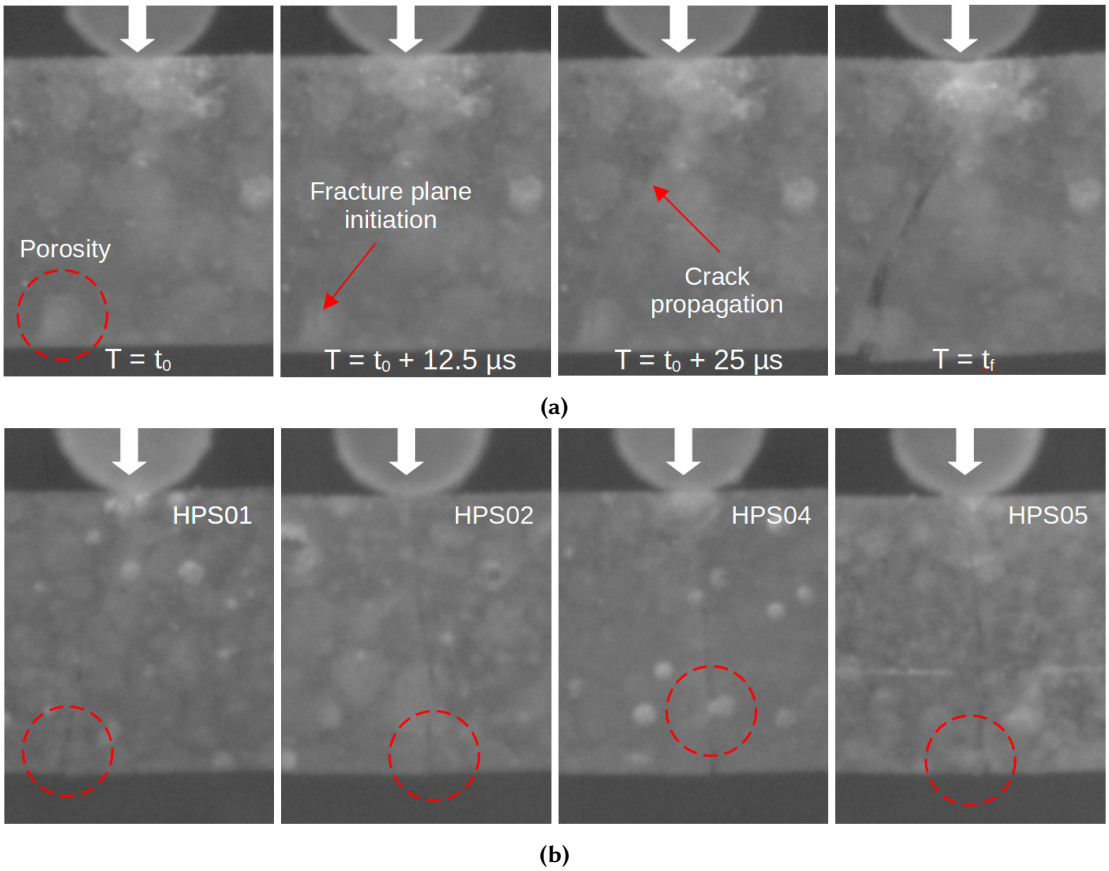

Figure 12: (a) Key moments of the HPS03 sample failure and (b) Pores suspected (red circles) to have triggered other HPS sample failure. Images are from the high-speed camera Phantom. The loading axis is symbolised by the white arrow on the upper support.

the interaction between defects during failure can be neglected. From (Weibull 1939), the failure probability P_f of a volume V for a given principal positive stress σ supposed to be uniformly distributed in the volume is:

$$P_f = 1 - exp(-\lambda_t V) \tag{4}$$

where λ_t represents the critical defect density.
In the three-parameters based Weibull distribution, this density is linked to the maximal positive principal stress by:

$$\lambda_t = \lambda_0 \left(\frac{\sigma - \sigma_u}{\sigma_0} \right)^m \tag{5}$$

where $\lambda_0 \sigma_0^{-m}$ is the so-called Weibull scale parameter. σ_u is the threshold stress under which the material does not fail.
A two-parameters distribution (i.e. $\sigma_u = 0$) often shows a good representation of the scattering of failure stresses, as observed by Danzer et al. 2007 for ceramics and more specifically by B. Parsons et al. 1992 for polycrystalline ice. Consequently the failure probability can be expressed as:

$$P_f = 1 - exp(-\lambda_0 V (\frac{\sigma}{\sigma_0})^m) \tag{6}$$

where the scale parameter ($\lambda_0 \sigma_0^{-m}$) and the Weibull modulus (m) are the two parameters describing the Weibull distribution.
The Weibull modulus is a dimensionless parameter representing the failure stress scattering. Materials with a high value of m tend to show a deterministic behavior whereas materials with a low value of m will present a more scattered failure stress distribution. The mean failure stress is further used to deduce the scale parameter by:

$$\sigma_w = \sigma_u + \sigma_0 (V \lambda_0)^{-1/m} \Gamma \left(\frac{m+1}{m} \right) \tag{7}$$

with Γ the gamma function, also known as the Euler integral of the second kind.

The corresponding standard deviation (σ_{sd}) is expressed according to:

$$\sigma_{sd}^2 = \sigma_0^2 (V\lambda_0)^{-2/m} \Gamma\left(\frac{m+2}{m}\right) - (\sigma_w - \sigma_u)^2 \tag{8}$$

As explained in (Forquin and Hild 2010), the ratio between the standard deviation and the mean failure stress corresponds to a continuously decreasing function of m bounded by the functions $1/m$ and $\pi/\sqrt{6}m \approx 1.29/m$.

The Weibull approach is classically used to characterize the defect population when a sample of a given volume V is subjected to a stress field up to failure. When this stress field is heterogeneous, such as during a bending test, an effective volume V_{eff} is considered in place of the volume V of the sample. The effective volume corresponds to the volume loaded by an uniform stress field for which the same level of maximum stress leads to the same failure probability as within V (Davies 1973). The effective volume thus depends on the stress field heterogeneity nearby the positive maximal stress and on the critical defect distribution in the sample. From Davies 1973, for three-points bending tests, the effective volume can be approximate by:

$$V_{eff} = \frac{V}{2(m+1)^2} \tag{9}$$

4.2 Determination of the Weibull parameters

Bending tests are frequently used to characterize the defect population supposed to be responsible for crack initiation during multiple fragmentation processes, as observed under dynamic loading (Forquin and Hild 2010). The Weibull model stands on the hypotheses that failure stresses of brittle materials under tensile loading in the quasi-static range are random. For a given stress, a sample has a probability P_f to break. This probability is related to two parameters: the stress field distribution in the volume and the properties of the defect population that contains the failure precursor. In this approach, the latter properties are characterized using the Weibull modulus. The Weibull modulus assumes that the defect population follows a Weibull distribution, thereby providing insights into the statistical distribution of defects within the material. In situations similar to our ice samples, where various defect populations (here pores) co-exist, we expect this approach to result into a statistical bias.

The least square method is probably the most used to determinate the Weibull modulus out of experimental tensile failure stresses. Other methods, such as the method of moments or of the maximum likelihood estimation exist and can be applied (see B. L. Parsons et al. 1991 for an overview on ice).

The first step consists in estimating an empirical cumulative distribution of failure probability from results of bending or tensile tests. To do so, experimental failure stresses are sorted in an ascending manner. For every failure stress, a rank i (integer) is attributed that corresponds to its position in the ranking. The empirical failure probability is then computed as:

$$P_f = \frac{i - 0.5}{N} \tag{10}$$

where N is the number of mechanical tests conducted.

It is thereafter possible to build the so-called Weibull diagram, where the inverse logarithm of the survival probability ($P_s = 1 - P_f$) is function of the applied stress. From the previous equations, it is expressed by:

$$ln(-ln(1 - P_f)) = mln(\sigma_m) + ln(V_{eff}\frac{\lambda_0}{\sigma_0^m}) \tag{11}$$

This equation implies that, when the strength scattering of the material follows a Weibull distribution, data can be interpolated by a linear function whose slope is the Weibull modulus. The scale parameter $\lambda_0 \sigma_0^{-m}$ is obtained from equation 7 once the mean failure stress is known.

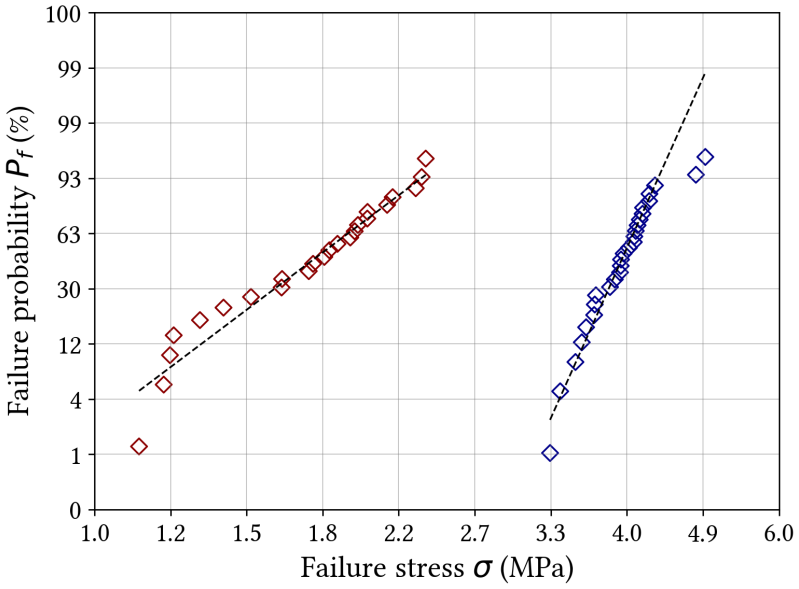

Figure 13: Cumulative distribution of experimental failure probabilities in function of HP (red markers) and LP (blue markers) samples failure stress. The black dotted lines represent the predictions of the Weibull model given by the equation 6, obtained by the least square method.

4.3 Weibull parameters for LP and HP ice samples

The least square method applied to the bending test results for ice samples LP and HP is illustrated in figure 13. Both HP and LP samples show a failure stress probability that can be reasonably approximated as varying linearly in the Weibull diagram, giving confidence in the application of the Weibull model. Please note that HPS samples (from the LaMCoS campaign) are not considered here since too few tests were performed to secure a robust statistical analysis. Keeping in mind the hypotheses behind the Weibull model, the determination of the modulus m was made after taking the following precautions. Failure stress of sample HP01 (σ_f = 0.69 MPa) is significantly weaker than the others and appears to be isolated on the Weibull diagram (point the closest to the origin). The defect responsible for the failure of this sample might have been of dimension out of the range of the active defect population of the other samples (see section 3.3). This sample was therefore not considered. Similarly, samples LP26 and LP27 show a higher failure stress than all other LP samples. The failure of these samples may well be due to the activation of a pore from a population of characteristic size smaller than all other LP samples.
By removing the data that appears out of the trend, we are more likely to characterize a specific defect population common to most of the samples studied, what therefore respects the frame of the Weibull model. The resulting mean failure stress therefore differs slightly from the one calculated in section 3.3 (cf table 3).

The Weibull parameters obtained from this analysis are given in table 3. They reveal a more deterministic behavior of LP samples than for HP samples ($m_{LP} >> m_{HP}$).

	m	$\lambda_0\ \sigma_0^{-m}$ ($m^{-3}\ Pa^{-m}$)	V_{eff} (m^3)	σ_w (MPa)	σ_{sd} (MPa)	α
HP	5.3	0.14×10^6	1.22×10^{-6}	1.76	0.37	0.97
LP	15.4	1.28×10^6	2.11×10^{-8}	3.89	0.28	0.99

Table 3: Weibull parameters of LP and HP microstructures, with m : Weibull's modulus, $\lambda_0\sigma_0^{-m}$: scale parameter, V_{eff} : effective volume, σ_w : mean stress to failure, σ_{sd} : standard deviation α : linear regression coefficient in Weibull's diagram.

By restricting the data used in this model approach to the ones with the closest value of failure stresses, we tried to select the samples for which only one of the three populations of pores identified in section 3.3 was containing the critical defect responsible for failure. Indeed, considering the dimensions of the samples, it is quite unlikely that the smallest pores (population

S) could have been responsible for failure. We therefore expect populations **M** and **L** for, respectively, LP and HP microstructures to have led to the failure of the samples.

In the In the following, we will go a step further in testing this hypothesis and the limits of applicability of the Weibull model by first providing a direct characterization of the defect population thanks to the μCT data (section 5) as made in (Forquin, Blasone, et al. 2021). We will then explore the volume effect associated with the heterogeneity of the defect populations in section 6.

5 Explicit estimation of the critical defect distribution from μCT measurements

The underlying hypothesis of the present study is that pores are the defects responsible for failure in our polycrystalline ice samples. μCT characterizations shown in section 2.3 therefore provide the exact defect distributions, in the limit of the resolution of the μCT apparatus.

In the following we will work in the frame of the linear elastic fracture mechanics and use the Griffith/Irwin failure criterion as done by Trustrum et al. 1983; Forquin, Rota, et al. 2004 or Danzer et al. 2007. The Griffith criterion considers that a crack of length $2a$ is unstable when the stress intensity factor K_I nearby the crack tip exceeds the fracture toughness K_{Ic} which is a material property. This statement writes:

$$\sigma_c = \frac{K_{Ic}}{Y\sqrt{\pi a}} \tag{12}$$

where Y is a theoretical shape parameter related to the crack geometry. It is bonded by two values $Y = 1$ and $Y = 2/\pi$, that correspond to theoretical situations (Sack 1946).

The fracture toughness K_{Ic} of ice has not been measured in the frame of this work but can be estimated from the literature. Fracture toughness values obtained from natural ice samples have been excluded due to the frequent lack of knowledge or control over the microstructure and impurity content in these samples, which can differ significantly from the laboratory ice studied here. Nixon et al. 1988 evaluated the fracture toughness on laboratory made polycrystalline ice samples, with microstructures similar to our LP samples. They measured the variation of K_{Ic} with the grain size and obtained values between 137 to 67 kPa.m$^{0.5}$ for grain sizes varying between 1.6 and 9.3 mm in diameter. The grain diameter of our samples being within 1 to 2 mm, the closest value would be the one obtained by Nixon et al. 1988 with 1.6 mm diameter grain size, that is $K_{Ic} = 91.3$ kPa.m$^{0.5}$. In brittle materials, K_{Ic} is expected to depend slightly on porosity. The only study we found that tested the impact of porosity on the fracture toughness of ice(Smith et al. 1990) reveals a wide scattering of the data. We will therefore neglect this effect on a first approximation, and keep the same value of K_{Ic} for both LP and HP samples.

Based on the pore distribution measured by μCT we can now relate a theoretical failure stress to the defect density with equation 12, (see figure 14). The shape parameter Y remains the only unknown of this approach. Since the real shape of pores in the samples is likely to be very different from the ideal crack shapes considered in the Griffith model, it is illusory to try to determine a value from observations. In figure 14, the relation between the defect density and the critical failure stress has been plotted for three values of Y. The prediction of the Weibull model obtained in section 4 (based on failure stress from bending tests), is superimposed on these plots. Y is selected so that the defect density matches the Weibull prediction at the experimental mean failure stress σ_w. The Y parameter thus obtained is of 1.1 for LP samples and of 0.8 for HP samples. Both values are very close to the ones found by Forquin, Blasone, et al. 2021 for a SiC ceramic and a Ultra-High Performance Concrete (UHPC).

Once all parameters have been set, the Griffith relation can in turned be used to specify, among the three pore populations that are observed in the samples, which one is more likely to have led to failure during the bending tests performed. The failure stresses measured are used to estimate a critical defect size that can be superimposed on the pore size distribution obtained from the μCT measurements, see figure 15. From this comparison, we confirm that critical defects are more likely to come from pores of population **M** for LP samples, while failure very likely

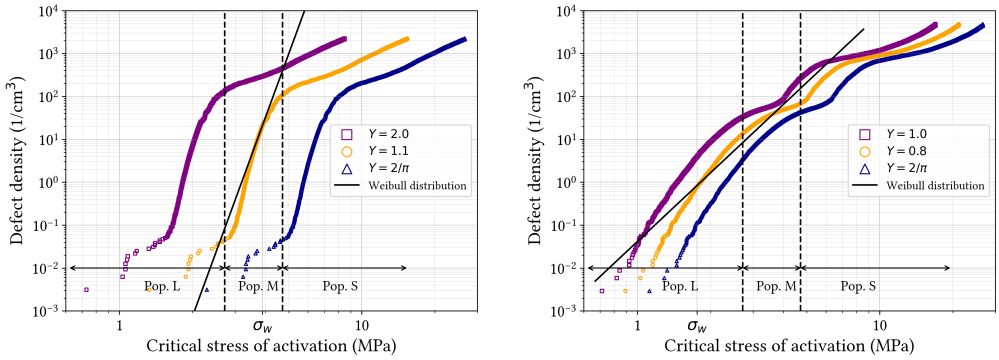

Figure 14: Calibration of the shape parameter Y. (a) Microstructure LP and (b) Microstructure HP. The yellow distributions correspond to the shape parameter chosen. The boundaries indicating the **S**, **M**, and **L** populations are valid only for $Y = 1.1$ (LP) and $Y = 0.8$ (HP).

comes from the activation of pores of population **L** for HP samples. These results are coherent with observations made on post-mortem samples (section 3).

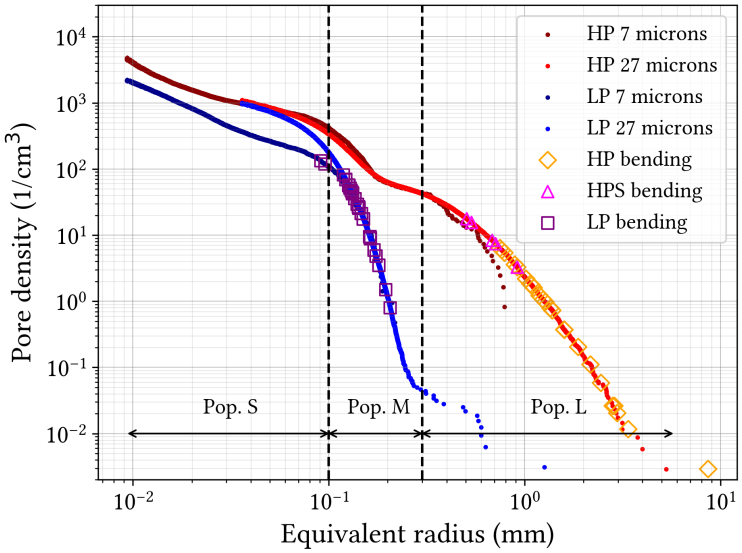

Figure 15: Cumulative pore size distribution with the highlight of pores suspected to initiate failure in bending samples.

At the end, the direct measurement of pore distributions from μCT can also be used to reveal the limitation and likely bias of the Weibull model which stands on the assumption of a Weibull distribution for the defect population. From figure 15 we extracted the likely range of pore sizes within which the active defect may stand ($[0.12 - 0.21\ mm]$ and $[0.75 - 3.38\ mm]$ for LP and HP samples respectively). In this range, the power-law relation between the defect density and the critical failure stress is well respected and leads to the estimation of a pseudo Weibull modulus that can be compared to the one obtained in section 4 based on the bending failure stresses measured experimentally (figure 16). The direct application of the Weibull model does not provide an accurate representation of the part of the defect distribution (population L) triggered in HP samples during bending tests. On the contrary, the prediction is very good for LP samples, what tends to show that the defects belonging to population M can indeed be characterized by a Weibull distribution.

6 Role of the effective volume

Estimating the defect population likely responsible for failure of a given material requires to make tensile experiments and to use the Weibull model as a first approximation. This procedure

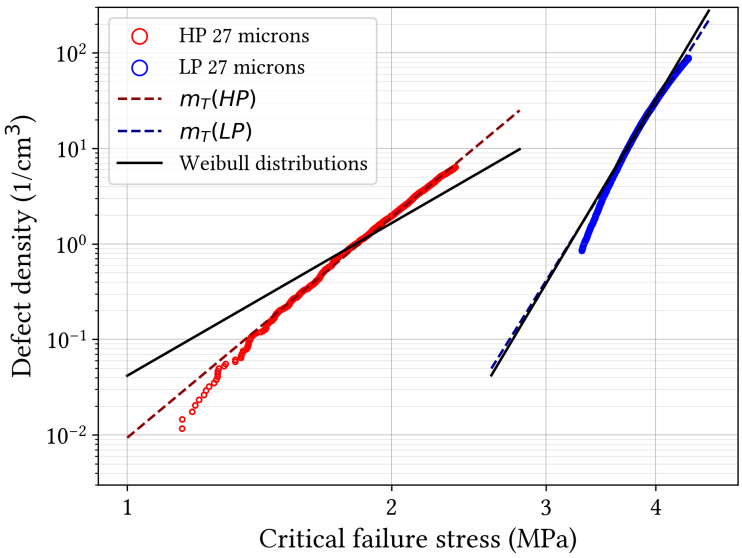

Figure 16: "Pseudo" Weibull modulus estimated from the pore size distribution of LP and HP samples. Weibull distributions for both type of samples are shown for comparison.

requires a first guest on the dimension of the active defect population in order to adjust the dimensions of the samples to be tested. When several defect populations co-exist in the materials, which is the case for LP and HP ices, it might require a large number of tests in order to cover the range of sample dimensions corresponding to the range of likely active defects sizes.

In the following, we make use of the 3D characterization of defect populations available for ice thanks to μCT in order to estimate the effect of a finite volume size on the failure stress estimation, for different active defect populations. In particular, by doing so, we are able to bond the limit of accuracy of the Weibull approach to evaluate the likely active defect population.

6.1 Influence of the sample volume on the failure stress

μCT analyses performed on our ice samples provide large volumes within which pores are located (in the limit of accuracy of the μCT apparatus). In the following, the large volumes will be called "initial volumes". Thanks to the SPAM software (see section 2.3), we are able to extract the exact coordinates (x, y and z) of the mass center for each pore resolved (down to a pore size about 3.43×10^{-6} mm^3 and 1.9×10^{-4} mm^3 for scans at 7 μm and 27 μm respectively).

To evaluate the volume effect described above, the initial volume is discretized into non-overlapping sub-volumes of cubic dimensions. These dimensions are varied between roughly 2 and 3800 mm^3 according to the properties of the initial volume, meaning its dimensions, the resolution at which it was analyzed, and the type of microstructure (LP or HP), see table 4, in order to secure the presence of a minimum of 30 pores in each sub-volume. Are available three initial volumes scanned at 27 μm for each LP and HP microstructures, and three initial volumes scanned at 7 μm for the LP microstructure, but only two for the HP microstructure. In order to remain statistically relevant, we needed to test a sufficiently high number of sub-volumes. A total of 24 sub-volumes are selected in each microstructure, and for each resolution. This number is close to the number of bending tests (25) conducted for each type of microstructure.

For each sub-volume, a failure stress was estimated from the Griffith criterion with the assumption that the largest pore is responsible for failure. See figure 17 for a schematic representation of the procedure.

6.2 Effective volume and mean failure stress

The evolution of the predicted mean failure stress as a function of the sub-volume size considered is plotted in figure 18 for both type of microstructure (LP and HP). Owing to the presence of pores of different size (coming from the different pore populations), sub-volumes of the same size present various failure stresses prediction resulting in a dispersion around the average value. On these graphs is also represented the prediction of the Weibull model (slope equal to $-1/m$ in

	LP microstructure		HP microstructure	
Voxel size	7 microns	27 microns	7 microns	27 microns
V_{tot} of initial volumes (mm^3)	600 + 700 + 800	3×105000	700 + 800	3×115000
Number of sub-volumes	3×8	3×8	2×12	3×8
Number of sub-volumes sizes	10	30	14	16
Size range of sub-volumes (mm^3)	[3.8 – 47]	[21 – 1100]	[2.0 – 29]	[49 – 3800]

Table 4: Parameters of the sub-volumes tested. V_{tot} is the size of the initial volumes available. The number of sub-volumes indicates the number of draws in the initial volumes for a given sub-volume size. The number of different sub-volume sizes considered as well as the size range of these sub-volumes are also given.

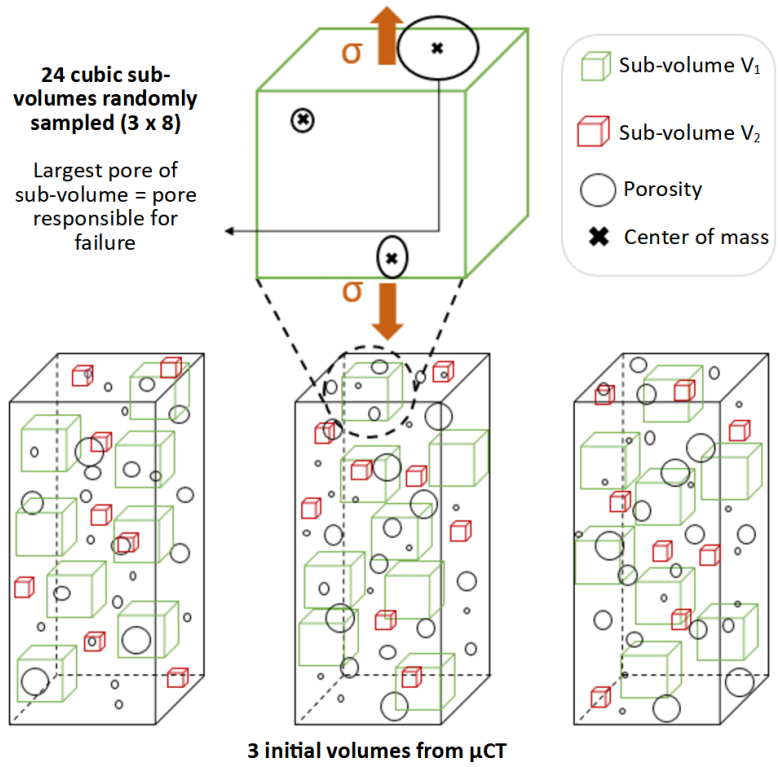

Figure 17: Sketch of the method used to estimate the failure strength on sub-volumes extracted from the exact microstructures. This sketch takes as example only two different sizes of sub-volumes.

log-log plot) as parameterized in section 4.3. The error bar associated with this prediction is the one corresponding to the standard deviation provided by equation 8.

We observe a good continuity between the prediction resulting from the initial volumes scanned at 27 μm and the ones scanned at 7μm. For both types of microstructure the predicted failure stress tend to increase when the sub-volume size decreases. This is coherent with the assumption that the smaller pores are the active defects. Nevertheless, a wider dispersion is predicted for smaller volumes, what reveals that more of those sub-volumes could have been necessary to achieve a better statistic.

The Weibull model offers a relatively good prediction for the HP microstructure (figure 18(a)) what is a bit counter-intuitive regarding the results of section 5. One explanation can be found in figure 14(b): if the Weibull distribution does not precisely represent the pores from population **L**, it does capture the overall trend for populations **L** and **M** put together, and it completely diverges for population **S**. As a result, the failure stress is completely underestimated for the smallest volumes considered when population **S** likely comes into play (see figure 19(b)).

The predicted response of the LP microstructure (figure 18(b)) is not as well reproduced by the Weibull model that slightly underestimates the response for the small sub-volumes but departs even more from the predicted response for the larger sub-volumes. The only good predictions of

the Weibull model are obtained for the sub-volumes whose response are close to the failure stress experimentally measured. Though the main defects activated in LP microstructure are from pore population **M** in all sub-volumes (figure 19(a)), and this population is supposed to be relatively well characterized by the Weibull parameters obtained from bending experiments (cf section 5). This divergence can be explain by the fact that, as show in figure 14(a), the Weibull distribution is not relevant for the full range range of pore size of population **M**. Largest pores from this population are not well modeled by the Weibull approximation.

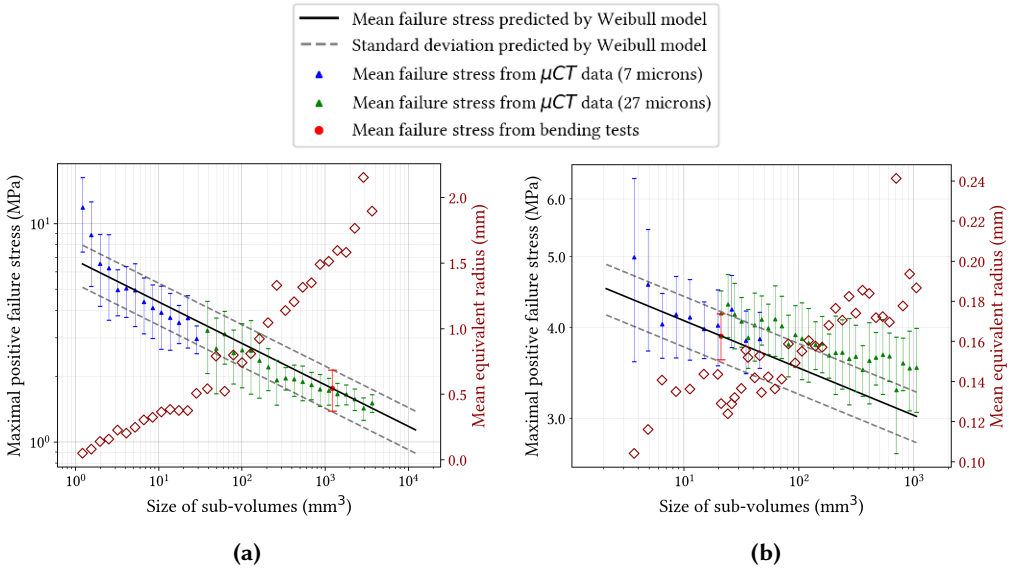

Figure 18: Evolution of the mean failure stress and the associated standard deviation with the size of the sub-volumes (*a*) HP and (*b*) LP microstructures. Results are compared with the predictions of the Weibull model.

7 Concluding remarks

First and foremost, the present work provides some of the few robust and reproducible data of bending failure in polycrystalline ice of well-constrained microstructure. Measured failure strengths are in the range 1.1 to 4.9 MPa, depending mostly on the porosity of the samples. Indeed, samples studied have been purposely spread into two families (by construction), a low porosity (LP) microstructure (~ 1 - 2%) and high porosity (HP) microstructure (~ 7 - 10%). The smallest strength values are found for the HP microstructure with σ_w = 1.76 ± 0.42 MPa while for the LP one, strengths are nearly twice as high with σ_w = 3.96 ± 0.37 MPa.

Both types of microstructures have been studied by means of micro-computed Xray tomography (μCT) that revealed three pore populations to co-exist in the samples, namely a small (r_{eq} < 0.1 mm), a medium (0.1 mm < r_{eq} < 0.3 mm) and a large (r_{eq} > 0.3 mm) pore population. LP samples contain only the small and medium size populations, while the HP samples contains all of them.

Although limited by the experimental complexity, high-speed camera images reveal that fracture often initiated at large pores in the HP samples (in LP samples, pores were too small for such an observation). Pores were therefore considered as the active defects in the bending experiments performed.

From this hypothesis we conducted an analysis of the link between the defect population distribution and the failure stress by mean of two approaches. The first one stands on the well-known Weibull model that uses bending failure stresses to estimate the active defect population in a given material. The second one is new and was already presented in (Forquin, Blasone, et al. 2021) and takes advantage of the 3D characterization of the microstructure by μCT in order to relates the defect characteristics to the failure stresses by means of the Griffith model.

The Weibull model is a statistical approach that stands on the hypothesis that the active defect population can be represented by a Weibull distribution. This is obviously not the case for

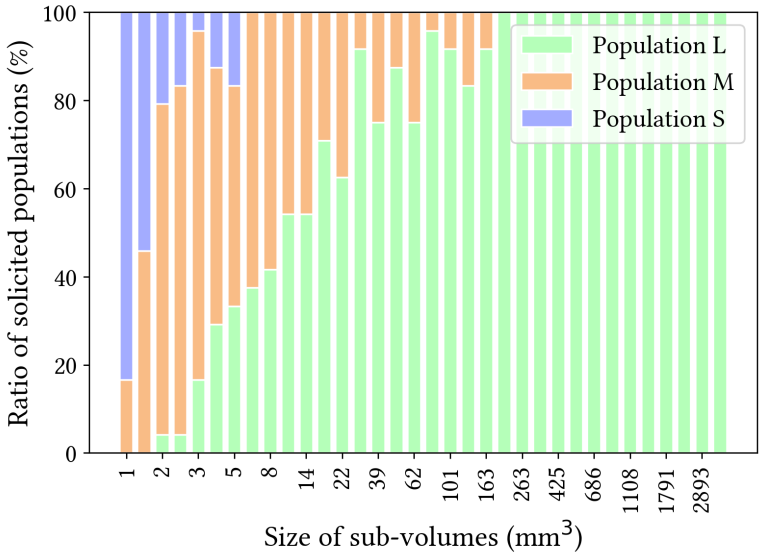

(a)

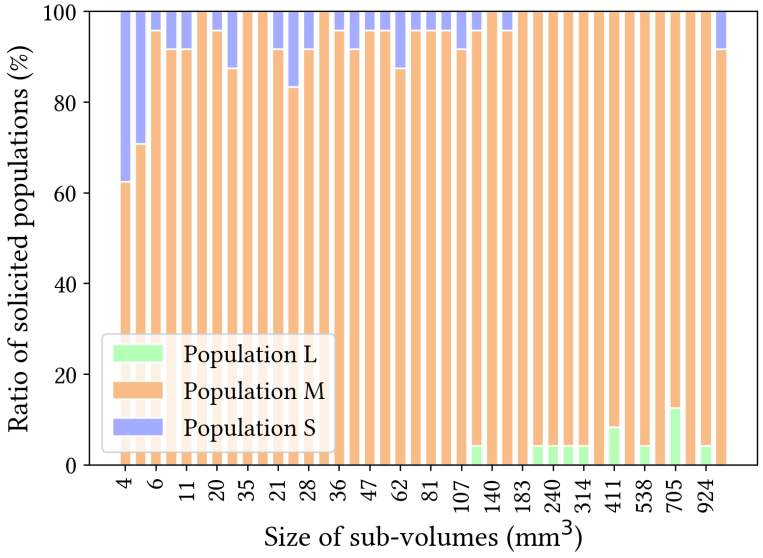

(b)

Figure 19: Proportion of the pore populations solicited in function of the sub-element size in the numerical simulations of tensile tests for (a) LP and (b) HP microstructures.

the pore distributions observed in our polycrystalline ice samples. We therefore expected the Weibull model to underestimate or overestimate the characteristics of the active defects when estimated only on the 25 or so bending strength experimentally measured. The comparison provided with the failure stresses estimated directly from the exact pore populations (exact in the limit of the μCT resolution) revealed that the Weibull model gave accurate predictions for LP samples. On the contrary, the range of pores activated in HP samples did not follow a Weibull distribution, questioning the relevance of applying the Weibull model when defect population distribution is non unimodal.

This issue has been explored by comparing the effects of the finite sample volume predicted by the Weibull model and by direct μCT measurements of pore distribution. Results showed that failure stresses predicted by both approaches are in agreements in the HP microstructure for the larger volumes. In small volumes, where the smallest pores may play a role, the prediction of the Weibull model is not correct anymore. For the LP microstructure, a slight divergence between the Weibull model and the predictions from the μCT measurements was noticed as soon as the volume considered differs from the experimental volume (the effective volume). These observations emphasize the difficulty to be confident on the Weibull model predictions when the

defect distribution is multi-modal and/or when a given defect population is not perfectly "Weibull distributed". The Weibull model predictions are limited to a specific range of defect dimensions and to the volumes that contain a statistically representative number of these defects. Care should therefore be taken when extrapolating the Weibull theory to situations where the effective volume varies, for instance under dynamic loading conditions.

At last, we have shown that the failure stress can be advantageously deduced from the defect populations when this latter is characterized explicitly by imaging techniques such as μCT as performed here. Indeed, providing that the Griffith criterion is applicable, a direct relation can be obtained between a given sample volume, the size of the active defects, and the resulting failure stress. Providing also that the defect dimensions are within the range of resolution of μCT characterizations, this method offers a good alternative to the Weibull approach. It also prevents from having to perform a too large number of experimental tests, on a large amount of samples of different volumes, to evaluate an robust failure strength.

Andò, E., R. Cailletaud, E. Roubin, and O. Stamati (2017). *the spam contributors, spam: The software for the practical analysis of materials*

Barnes, P., D. Tabor, and J. Walker (1971). "The friction and creep of polycrystalline ice". *Proc. R. Soc. Lond. A* 324.1557, pp. 127–155

Danzer, R., P. Supancic, J. Pascual, and T. Lube (2007). "Fracture statistics of ceramics–Weibull statistics and deviations from Weibull statistics". *Engineering Fracture Mechanics* 74.18, pp. 2919–2932

Davies, D. (1973). "The statistical approach to engineering design in ceramics". *Proceedings of the British Ceramic Society*. Vol. 22, pp. 429–452

Druez, J., J. Cloutier, and L. Claveau (1987). "Étude comparative de la résistance à la traction et à la compression de la glace atmosphérique". *Le Journal de Physique Colloques* 48.C1, pp. C1–337

Forquin, P., M. Blasone, D. Georges, and M. Dargaud (2021). "Continuous and discrete methods based on X-ray computed-tomography to model the fragmentation process in brittle solids over a wide range of strain-rates-application to three brittle materials". *Journal of the Mechanics and Physics of Solids* 152, p. 104412

Forquin, P. and F. Hild (2010). "A probabilistic damage model of the dynamic fragmentation process in brittle materials". *Advances in applied mechanics*. Vol. 44. Elsevier, pp. 1–72

Forquin, P., L. Rota, Y. Charles, and F. Hild (2004). "A method to determine the macroscopic toughness scatter of brittle materials". *International Journal of Fracture* 125.1, pp. 171–187

Georges, D., D. Saletti, M. Montagnat, P. Forquin, and P. Hagenmuller (2021). "Influence of porosity on ice dynamic behavior as assessed by spalling tests". *Journal of Dynamic Behavior of Materials*

Hawkes, I. and M. Mellor (1972). "Deformation and fracture of ice under uniaxial stress". *Journal of Glaciology* 11.61, pp. 103–131

Ikeda, S., T. Nakano, and Y. Nakashima (2000). *Three-dimensional study on the interconnection and shape of crystals in a graphic granite by X-ray CT and image analysis*

Jayatilaka, A. d. S. and K. Trustrum (1977). "Statistical approach to brittle fracture". *Journal of Materials Science* 12.7, pp. 1426–1430

Nixon, W. A. and E. Schulson (1988). "The fracture toughness of ice over a range of grain sizes"

Parsons, B., M. Lal, F. Williams, J. Dempsey, J. Snellen, J. Everard, T. Slade, and J. Wlliams (1992). "The influence of beam size on the flexural strength of sea ice, freshwater ice and iceberg ice". *Philosophical Magazine A* 66.6, pp. 1017–1036

Parsons, B. L. and M. Lal (1991). "Distribution parameters for flexural strength of ice". *Cold regions science and technology* 19.3, pp. 285–293

Petrovic, J. (2003). "Review mechanical properties of ice and snow". *Journal of materials science* 38.1, pp. 1–6

Sack, R. (1946). "Extension of Griffith's theory of rupture to three dimensions". *Proceedings of the Physical Society (1926-1948)* 58.6, p. 729

Schulson, E. M. (2001). "Brittle failure of ice". *Engineering fracture mechanics* 68.17-18, pp. 1839–1887

Schulson, E. M. and P. Duval (2009). *Creep and fracture of ice*. Cambridge University Press

Schulson, E. M., P. Lim, and R. Lee (1984). "A brittle to ductile transition in ice under tension". *Philosophical Magazine A* 49.3, pp. 353–363

Schwarz, J., R. Frederking, V. Gavrillo, I. Petrov, K.-I. Hirayama, M. Mellor, P. Tryde, and K. Vaudrey (1981). "Standardized testing methods for measuring mechanical properties of ice". *Cold Regions Science and Technology* 4.3, pp. 245–253

Smith, T., M. Schulson, and E. Schulson (1990). "The fracture toughness of porous ice with and without particles". *Proceedings, Ninth International Conference on Offshore Mechanics and Arctic Engineering*, pp. 241–246

Timco, G. et al. (1994). "Flexural strength equation for sea ice". *Cold Regions Science and Technology* 22.3, pp. 285–298

Timco, G. and W. Weeks (2010). "A review of the engineering properties of sea ice". *Cold regions science and technology* 60.2, pp. 107–129

Tozawa, S. and Y. Taguchi (1986). "A preliminary study of scale effect on structural strength of ice specimen". *International offshore mechanics and arctic engineering. Symposium. 5*, pp. 336–340

Trustrum, K. and A. D. S. Jayatilaka (1983). "Applicability of Weibull analysis for brittle materials". *Journal of Materials Science* 18.9, pp. 2765–2770

Weibull, W. (1939). "A statistical theory of strength of materials". *IVB-Handl.*

Wilson, C. J., D. S. Russell-Head, and H. M. Sim (2003). "The application of an automated fabric analyzer system to the textural evolution of folded ice layers in shear zones". *Annals of Glaciology* 37, pp. 7–17

Funding This work was supported by:

- the Brittle's Codex chair (Fondation UGA).
- the CEA-CESTA
- The AITA was co-funded by the Labex OSUG@2020 (ANR 10 LABEX 56)
- The TomoCold facility was funded by CNRM, LabEx OSUG@2020 (ANR 10 LABEX 56) and the french national programme LEFE/INSU.

Acknowledgements We are very grateful to David Hébert and Jean-Luc Rullier from CEA-CESTA for their support, curiosity and feedbacks provided all along the project. We thank Jacques Roulles for its support with the cold room facility at CEN-CNRM.

Authors' contributions DG carried out most of the study, performed experimental measurements, data treatment and analyses, numerical modeling, and drafted the manuscript. DS helped with the experimental tests and the data treatment and analyses. MM participated to the sample preparation, the experimental tests, the data analyses and wrote most of the paper with DG. PF developed the experimental procedure and the numerical approach and participated to the data analyses. HM provided access to the experimental equipment and his support in LaMCoS. All authors provided critical review of the manuscript. All authors read and approved the final manuscript.